The Importance of Single-Mode Behavior in Silicon-On-Insulator Rib Waveguides With Very Large Cross Section for Resonant Sensing Applications

Antoine Leblanc-Hotte, Jean-Sébastien Delisle, Sylvie Lesage, and Yves-Alain Peter

***Abstract*—Control of light properties through propagation in large cross section optical rib waveguides is of utmost importance to obtain the desired behavior, especially with resonant cavities. We have simulated, fabricated, and experimentally tested optical rib waveguides to evaluate the advantages of single-mode properties against multimode. Modal analysis of very large cross section rib waveguides showed that only particular dimensions allow a single-mode behavior. Furthermore, on-chip Fabry–Perot cavities were coupled to rib waveguides to assess impacts for a typical resonator. Experimental results are in good agreement with simulation guidelines, effectively highlighting the importance of single-mode behavior for resonant sensing applications.**

***Index Terms*—Microphotonics, rib waveguide, sensing, single-mode.**

I. Introduction

MICROPHOTONICS technologies find numerous applications in the biomedical and chemical fields. A growing number of devices using on-chip integrated microphotonic structures are being designed as tools to facilitate the work of specialists in biology and medicine. These structures can use evanescent waves of an optical waveguide as a sensor [1], arrayed waveguide grating for multiplexed sensing [2] or even take advantage of optical resonant cavities for enhanced photon life time [3]. Integrated sensors combining microfluidics and microphotonics commonly use waveguides to bring light from optical fibers to the on-chip sensing structure. Control over light properties through waveguide propagation is of utmost importance to obtain the desired behavior, especially with resonant cavities. As an example, previous work reported a microfabricated optical waveguide coupled to a Fabry–Perot resonant cavity for single cell sensing with abnormally high losses [4]. This device employed a resonant spectroscopic measurement which exploits small differences in cells refractive index. This measurement can improve the discriminative resolution of medical devices used for diagnosis, such as flow cytometers, for more reliable cellular identification. It could also permit the identification of new cellular parameters or even novel cell types.

Large particle analysis, as in [4] with cells of approximately 10–12 μm in diameter, requires waveguides of at least a few micrometers in height. However, on-chip rib waveguides made out of silicon exhibit large refractive index difference with its cladding (air). Consequently, waveguides with large dimensions and high core-cladding refractive index difference theoretically support multiple optical modes. In this paper, we suggest that single-mode rib waveguides yield optical properties better suited for resonating sensors spectroscopy. Indeed, propagation of two or more modes in a waveguide with close modal refractive index generates a beating effect. Thus, modal power distribution at a fixed length is different for each wavelength, which renders a non-uniform spectrum and hides resonance peaks in its background. Moreover, since the optical path in a coupled cavity changes with the presence of a particle, the whole beating pattern also changes making very hard deducing the resonator response. Finally, the intensity measurement based on peak shifting reported in [4] is better suited for a smooth slope of the resonance. Even if multimode resonances occur at the same wavelength for a Fabry–Perot, the total peak profile is composed of multiple resonances each possessing a different height, Full Width at Half Maximum (FWHM) and slope. This yields a final peak shape and resonance sensitivity not suitable for practical measurements.

It has been shown previously first by Soref [5] and then by Pogossian [6] that rib waveguides on Silicon-On-Insulator (SOI) with a cross-section of a couple micrometers (around 4 μm $\times$ 4 μm) can be effectively defined as single-mode. In these particular cases, interpretation of the single-mode behavior for an optical rib waveguide must be carefully defined. In theory, these waveguides support more than one mode, making them multimode by definition. However, after one or two millimeters of propagation only the fundamental mode remains because losses for higher order modes are superior. This phenomenon makes these studied optical rib waveguides practically

Manuscript received December 16, 2015; revised March 8, 2016; accepted March 21, 2016. Date of current version. This work is supported in part by the Natural Sciences and Engineering Research Council of Canada PGSD3-445848-2014, the Fonds de recherche du Québec—Nature et technologies Equipe 173638 and RQMP 187779.

A. Leblanc-Hotte is with the Department of Engineering Physics, École Polytechnique de Montréal, Montreal, QC H3T 1J4, Canada (e-mail: antoine.leblanc-hotte@polymtl.ca).

J.-S. Delisle is with the Division of Hematology-oncology, Department of medicine, Centre de recherche de l'Hôpital Maisonneuve-Rosemont, Université de Montréal, Montreal, QC H1T 2M4, Canada (e-mail: js.delisle@umontreal.ca).

S. Lesage is with the Department of Microbiologie, Infectiologie et Immunologie, Centre de recherche de l'Hôpital Maisonneuve-Rosemont, Université de Montréal, Montreal, QC H1T 2M4, Canada (e-mail: sylvie.lesage@umontreal.ca).

Y.-A. Peter is with the Department of Engineering Physics, École Polytechnique de Montreal, Montreal, QC H3T 1J4, Canada (e-mail: yves-alain.peter@polymtl.ca).

Digital Object Identifier 10.1109/JSTQE.2016.2545634

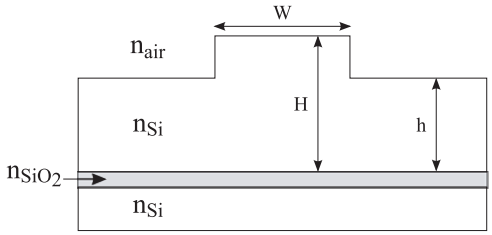

Fig. 1. Rib waveguide on SOI cross-section dimensions and variables used for modal analysis.

single-mode for experimentations. Then, Lousteau [7] showed that for slightly higher rib waveguides (around 7.5 μm) single-mode behavior is not as simple as following the established design rules by Soref and Pogossian. Therefore, precaution must be taken when working with large cross-section optical rib waveguides. We have tested this theory and evaluated the advantages of single-mode properties against multimode for resonators. We have simulated, fabricated and experimentally tested isolated rib waveguides as well as coupled to a typical resonating cavity: an integrated in-plane Fabry–Perot. This paper reports simulation, fabrication and optical characterization of very large cross-section optical rib waveguides on SOI for resonant sensing applications.

II. Rib Waveguide Modal Analysis

This section describes the technique used for modal analysis of the rib waveguides and reports the results obtained for different dimensions. The cross-section dimensions of the rib waveguide are defined in Fig. 1 where W is the width of the rib, H is the total height of the rib and h is the height of the surrounding slab. Refractive indices for air, silicon, and silicon dioxide (SiO_2) are represented by the common variable n and their respective subscript. In this design, air is the top cladding, silicon dioxide is the bottom cladding and silicon is the core of the rib waveguide. Equations (1) and (2) are the proposed formulas for design purposes established by Soref [5] and later corrected by Pogossian [6]. These equations need to be jointly satisfied in order to have a single-mode behavior of the rib waveguide

$$\frac{h}{H} \geq 0.5 \tag{1}$$

$$\frac{W}{H} \leq \alpha + \frac{h/H}{\sqrt{1-(h/H)^2}} \tag{2}$$

where $\alpha = 0.3$ for Soref's formulation and $\alpha = 0$ with Pogossian's correction. The variables h/H and W/H are introduced for uniformity with other published work [5]–[7].

Performed simulations are based on the technique used by Lousteau [7]. We used a standard Finite Difference method to design the waveguide geometry and a direct matrix mode solver with Perfectly Matched Layers as boundary conditions. This method outputs the complex refractive index of the supported modes and the imaginary part was used to calculate the modes respective attenuation coefficient. We follow Lousteau's notation for rib waveguide modes: HE_{nm} and EH_{nm}. Where HE modes are horizontally polarized (quasi-transverse-electric (TE)) and EH modes are vertically polarized (quasi-transverse-magnetic (TM)). For compactness, we only discuss horizontally polarized modes, HE, without loss of generality. Modes with pure vertical symmetry are represented with $m = 0$ whereas modes with $n = 0$ have pure horizontal symmetry. Also, we have voluntarily disregarded horizontally symmetric modes, HE_{0m}, assuming that they couple into the slab and do not propagate [7]. Furthermore, modes with an odd integer n were disregarded considering simulation results. These modes never reach an attenuation coefficient low enough to add meaningful information to the final attenuation map. Finally, we have stopped our investigation to the HE_{40} mode since higher order modes are considerably affected by the surface roughness in the propagation direction and do not have enough power coupled into them. This study evaluates single-mode advantages for resonant sensing application over multimode and is not intended to be an exhaustive modal analysis of optical rib waveguides. Therefore modes order higher than HE_{40} would not be meaningful in this case.

In this work, the value of H was fixed to 15 μm considering a biomedical sensing application and typical cells diameter. Values of h/H ranged from 0.5 to 1 whereas values of W/H ranged from 0.25 to 1.33. Operating wavelengths were chosen to be $\lambda_1 = 1.50$ μm, $\lambda_2 = 1.575$ μm, and $\lambda_3 = 1.65$ μm covering a large part of the near infrared (NIR) transparent region for silicon. The losses recorded for HE_{20} and HE_{40} modes were then computed and reported in an attenuation coefficient map. Fig. 2 reports the lowest attenuation coefficients recorded, out of the three simulated wavelengths, in function of the h/H and W/H ratios for a) the HE_{20} mode, b) the HE_{40} mode, and c) both modes combined. Dark regions in these maps represent high attenuation of the corresponding optical modes over the three wavelengths. Thus, for combined HE_{20} and HE_{40} modes, black regions highlight geometries for which the fundamental mode should be dominant (Fig. 2(c)). As references, Soref's and Pogossian's boundary condition are also plotted onto these graphics, single-mode behavior is expected below the boundary condition.

Accordingly with Lousteau's conclusion, simulation results of Fig. 2(c) tends to advise that *"satisfying the design formulas (1) and (2) is not in itself sufficient to ensure effective single-mode operation"* [7]. To further test this theory, we fabricated on-chip stand-alone rib waveguides to assess the predicted behaviors. Additionally, rib waveguides coupled to an integrated in-plane Fabry–Perot cavity were simultaneously fabricated to evaluate the effect in a resonant cavity. Since all structures are microfabricated in a single process, the slab height h is the same for all rib waveguides, thus only the width W was varied. Chosen geometries are represented by black (or white for better contrast) dots in Fig. 2(c). These four geometries are correlated to: one multimode rib waveguide according to Pogossian's formula and to our simulation (top dot with $W \geq H$), one multimode rib waveguide according to our simulation but single-mode in Pogossian's theory (second dot from top with $W = H$), and two rib waveguides less multimode, i.e. with potential single-mode like behavior, according to our simulations and single-mode according to Pogossian (third from top with $W = H/2$ and bottom dot with $W = H/3$).

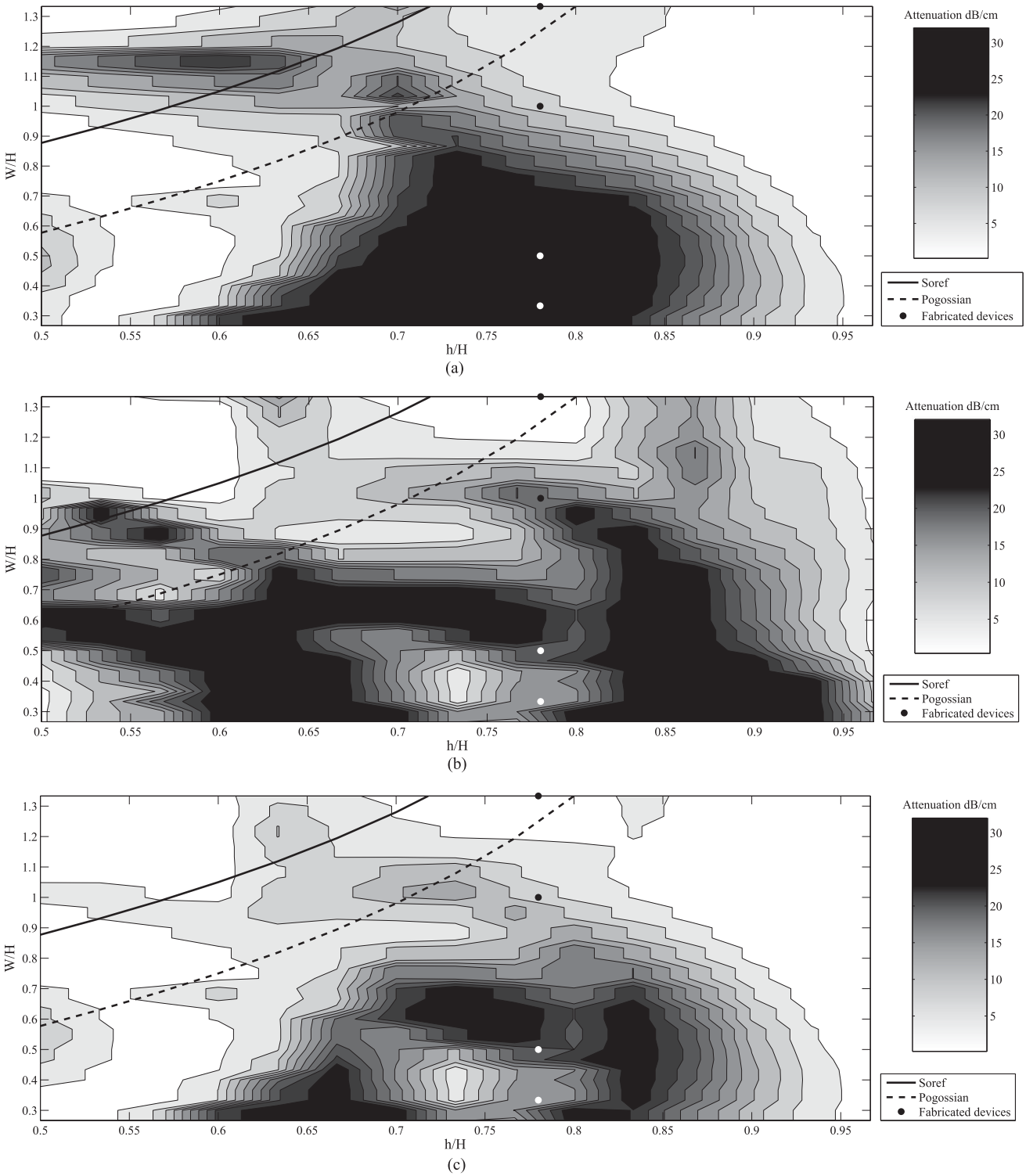

Fig. 2. Lowest attenuation coefficient recorded for (a) HE_{20} mode, (b) HE_{40} mode, and (c) combined HE_{20} and HE_{40} at all simulated operating wavelengths in function of ratios *h/H* and *W/H*. Plain line corresponds to Soref's single-mode boundary whereas the dashed line is associated to Pogossian's correction.

III. Microfabrication

A SOI wafer with a 600 μm handle, 0.5 μm oxide layer, and 15 μm silicon top layer was employed. Final devices are achieved in a two-phase production which both includes standard photolithography and Deep Reactive Ion Etching (DRIE). In the first microfabrication phase, Fabry–Perot cavities are photolithographically defined and etched down to the buried oxide layer using a DRIE-BOSCH process with alternating SF_6 and C_4F_8 plasmas. These Fabry–Perot cavities are composed of two Distributed Bragg Reflectors (DBRs) facing one another and separated by a microfluidic channel acting as the cavity gap. Design and microfabrication of the DBRs was based on

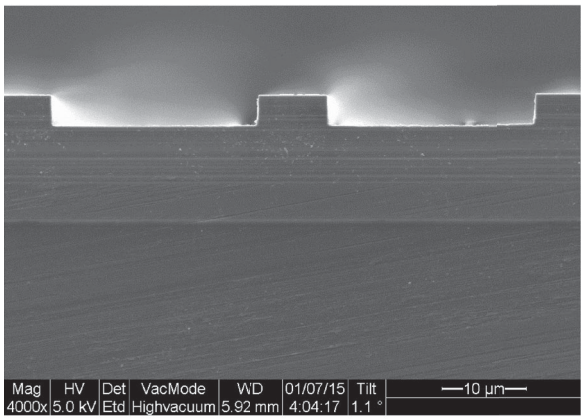

(a)

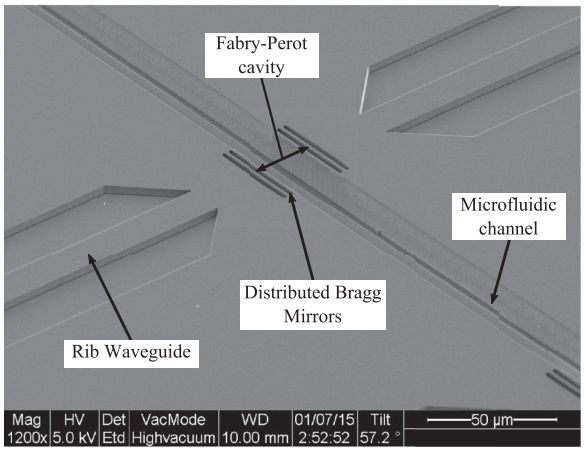

(b)

Fig. 3. SEM images of a microfabricated device showing (a) rib waveguide facet geometry and (b) structure of a rib waveguide coupled to a Fabry-Perot cavity composed of two DBRs.

previously published work [8]. In the second phase, rib waveguides are photolithographically defined and etched with the same DRIE-BOSCH process but at a lower depth to achieve the rib geometry. The SOI wafer is subsequently cut into separate chips using a dicing saw (ADT, Provectus 7100) and an engineered resin/diamond blade yielding diced facets of optical quality. Roughness measurement on these facets reported a mean value of 5.5 nm which provides low scattering losses for coupling. Then, the separated devices are cleaned in a piranha solution (H_2SO_4 + H_2O_2) followed by a final decontamination in oxygen plasma. Fig. 3 shows scanning electron microscopy (SEM) images of a microfabricated rib waveguide facet geometry and a Fabry–Perot cavity structure. Measurements reported a value of $h = 11.7$ μm for all waveguides, widths of 5, 7.5, 15, and 20 μm (all within ± 250 nm) and waveguides length of 7.5 mm.

IV. Experimental Setup

In this study, two different experimental setups were used: one to analyze the output NIR mode profile of the rib waveguide and another to analyze the spectral response from the photonic structure. In both cases, stand-alone and Fabry–Perot cavity coupled rib waveguides were experimentally tested. The NIR mode profile analysis setup uses a wide band laser source (Newport, BBS-430) with a standard SMF-28 fiber output butt coupled into the rib waveguide inlet facet. At the output facet, a mirror is set at angle of 45° from the horizontal axis to reflect NIR light to an InGaAs camera (VDS Vosskhler GmbH, NIR-610PGE) through an objective lens. Camera exposure time was set to allow small features of the mode profile to be spatially defined. The spectral analysis setup uses the same wide band laser source jointly with standard SMF-28 optical fibers butt coupled in and out of the rib waveguide. This setup difference resides in the fact that an optical spectrum analyzer (Hewlett Packard, 86142A) collects the NIR light and records the differential spectrum (raw spectrum normalized with the reference signal) on a log scale in dB units.

V. Results and Discussion

NIR mode profile analyses as well as spectral analyses for the four fabricated stand-alone rib waveguides geometries are reported in the first section. In addition, both analyses are presented for these selected rib waveguides coupled to a Fabry–Perot cavity in the second section. The last section reports Fabry–Perot resonance properties for single-mode like rib waveguide.

A. Stand-Alone Rib Waveguide

1) NIR Mode Profile: Fig. 4 shows the different output NIR mode profiles, after a propagation of 7.5 mm, in their respective stand-alone rib waveguide geometry. Features of the output NIR mode profile images of Figs. 4(a), (b), (c), and (d) show that rib waveguides widths of 20, 15, 7.5, and 5 μm respectively, present a higher order optical mode at the end facet. In all cases, the captured mode profile is similar to the one of a HE_{40} mode. It is important to point out that exposure time of the infrared camera was lowered until small features of higher order optical modes could be seen even if multiple modes are simultaneously present, including the fundamental one.

2) Spectral Analysis: Fig. 5 shows the output spectra of the different stand-alone rib waveguide widths. These spectra show arbitrary variation of intensity in function of wavelength. The amplitude of these variations for Figs. 5(a) and (b) is estimated to be around 13 dB whereas for Figs. 5(c) and (d) it is estimated to 3.5 dB.

For multimode rib waveguides, a beating effect between propagating modes is expected. Since the characteristic beating length is dependent on the propagating wavelength, a fixed length waveguide will output more or less power in the fundamental mode. Because the output light is butt coupled into a single-mode optical fiber, most collected light power will come from the fundamental mode. Thus, recorded intensity in function of wavelength for highly multimode rib waveguides are expected to show more variation than practical single-mode waveguides. In the cases of rib waveguides width of 7.5 and 5 μm, spectral measurements exhibits less variation, associated to single-mode like behavior, whereas NIR mode profile images

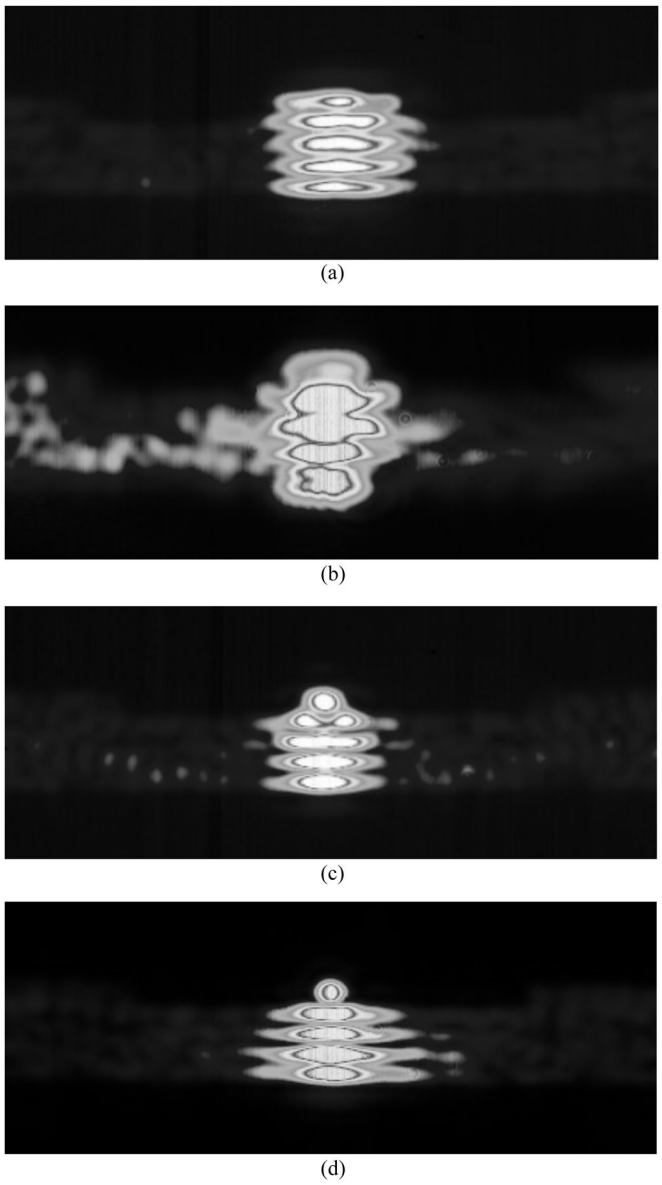

Fig. 4. NIR images of the output mode for stand-alone optical rib waveguides showing presence of higher order mode profile for widths of (a) 20 μm, (b) 15 μm, (c) 7.5 μm, and (d) 5 μm, respectively.

show a higher order profile. These geometries correspond to greater losses than other fabricated waveguides for both simulated HE_{20} and HE_{40} modes as shown in Fig. 2(c). Thus, even if higher order mode features can be seen in the NIR mode profile image, most of the power remains in the fundamental mode for all recorded wavelengths. Based on results from Figs. 4 and 5 rib waveguides with widths of 20 and 15 μm are practically multimode whereas rib waveguides of widths 7.5 and 5 μm can be considered as practically single-mode.

B. Rib Waveguide Coupled to a Fabry–Perot Cavity

1) NIR Mode Profile: Fig. 6 shows the NIR output mode profiles for Fabry–Perot cavity coupled rib waveguides with different geometries. Features of the mode profile images for

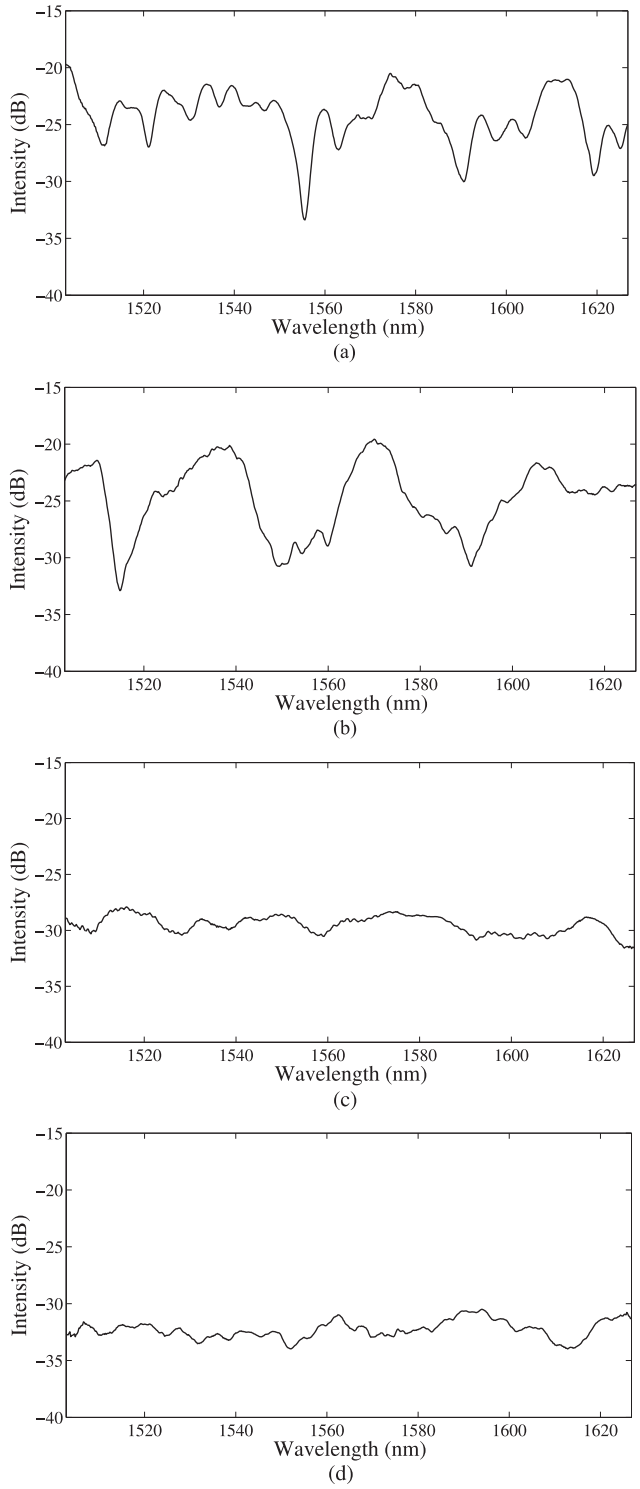

Fig. 5. Output spectra for stand-alone optical rib waveguides showing intensity variation for widths of (a) 20 μm, and (b) 15 μm, whereas widths of (c) 7.5 μm and (d) 5 μm exhibits lower fluctuations.

Figs. 6(a), (b), and (c) show that rib waveguides widths of 20, 15, and 7.5 μm, respectively, present higher order optical modes profile at the end facet. On the other hand, Fig. 6(d) for a rib waveguide width of 5 μm exhibits features similar to a single-mode like profile. The cavity coupled rib waveguide output mode profiles are different from each other unlike stand-alone

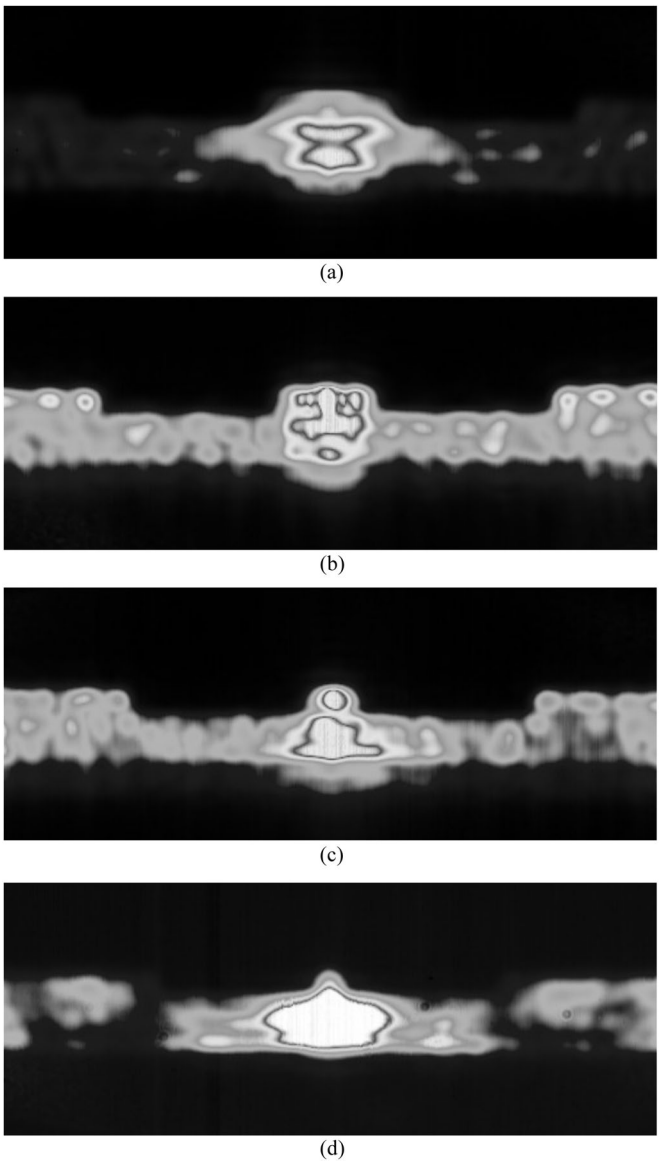

Fig. 6. NIR images of the output mode for cavity coupled rib waveguides showing higher mode profile for widths of (a) 20 μm, (b) 15 μm, and (c) 7.5 μm and single-mode profile for width of (d) 5 μm.

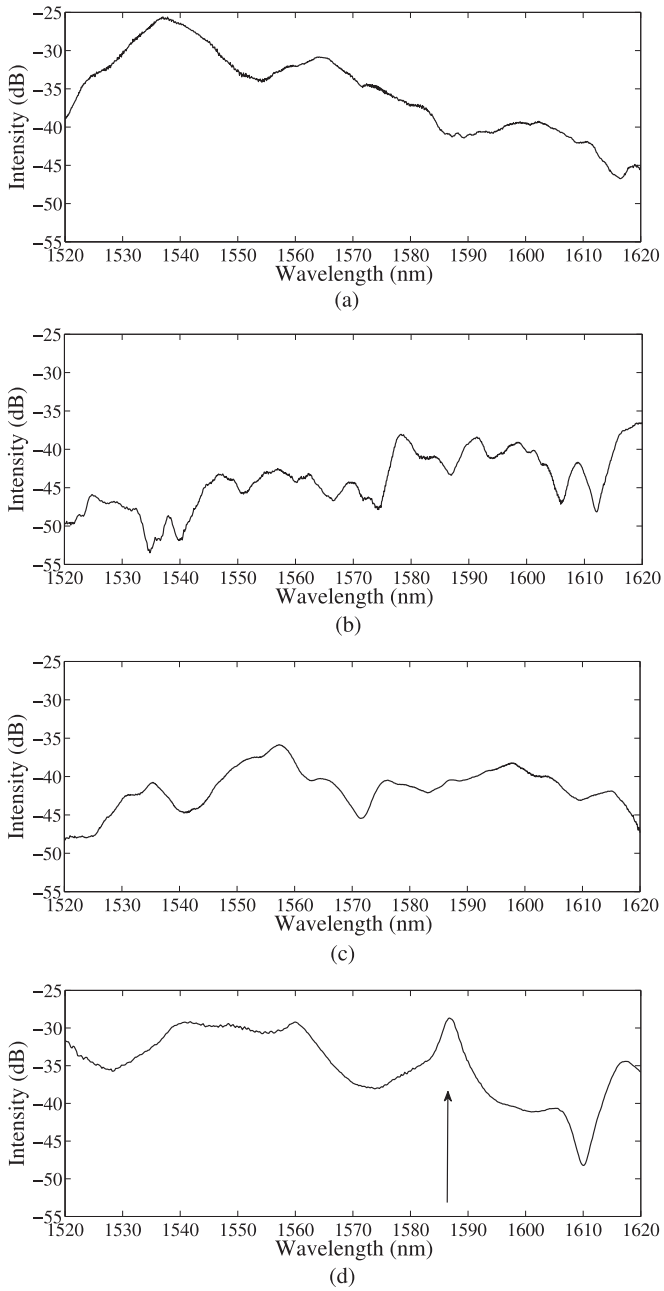

Fig. 7. Output spectra for Fabry-Perot cavity coupled rib waveguides showing intensity profile for widths of (a) 20 μm, (b) 15 μm, and (c) 7.5 μm and exhibiting an isolated resonance peak for a width of (d) 5 μm.

rib waveguide ones in Fig. 4. Indeed, the Fabry–Perot's DBRs roughness, inherited from the DRIE-BOSCH process's scalloping, mainly lowers higher order optical modes relative intensities and contrasts. Consequently, the infrared camera renders a more noticeable superimposition of optical modes.

2) Spectral Analysis: Fig. 7 presents the output spectra for Fabry–Perot cavity coupled rib waveguides with different geometries. For rib waveguide widths of 20, 15, and 7.5 μm the spectra do not exhibit easily identifiable resonance peak. The intensity in function of wavelength seems erratic and presents no useful information as a resonant sensor device. On the other hand, the spectrum on Fig. 7(d) for a width of 5 μm exhibits an isolated resonance peak, identified by an arrow.

These results for resonant cavity coupled rib waveguides support the initial hypothesis that only single-mode behavior enables identifiable resonance peaks and provide useful information. Indeed, on-chip integrated silicon multimode rib waveguides tend to generate beating between supported propagating modes and render a complex spectrum without even being conjugated to a resonant cavity. When coupled, the cavity's resonance peaks are "lost" in the intensity variations background, thus not identifiable, and no sensing features can be extracted *a priori*. Therefore, achieving single-mode like behavior in integrated rib waveguides, with very large cross-section, coupled to a resonant cavity is crucial. To our knowledge, this paper reports the first study to experimentally achieve it.

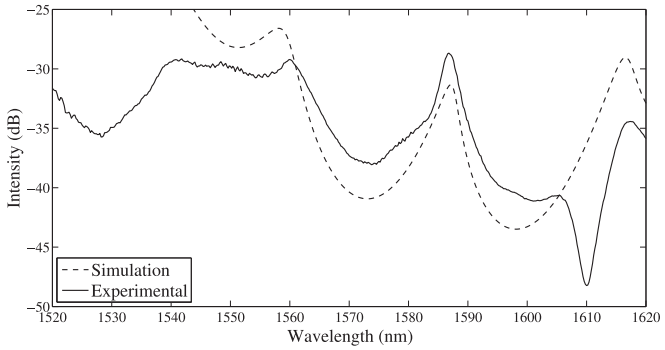

Fig. 8. Spectral comparison between simulated, dashed line, and experimental, plain line, single-mode Fabry–Perot cavity for a rib waveguide width of 5 μm.

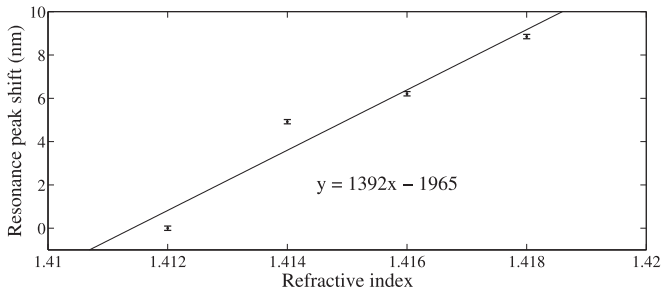

Fig. 9. Measurement points for single-mode cavity coupled rib waveguide resonance peak displacement with certified refractive index oils superposed with a linear fit.

TABLE I
FABRY–PEROT RESONANCE PROPERTIES CALCULATED FROM THE EXPERIMENTAL SPECTRA FOR A RIB WAVEGUIDE WIDTH OF 5 μm

	Experimental	Simulated
Loss at maximum (dB)	−28.7	−31.3
FWHM (nm)	3.56	4.41
FSR (nm)	30.6	29.3
Finesse	8.6	6.6
Sensitivity (nm/RIU)	1392	N/A
Resolution (RIU)	1.1×10^{-5}	N/A

C. Fabry–Perot Resonance Properties

In this section, information on the Fabry–Perot resonance peak for single-mode cavity coupled rib waveguide with a width of 5 μm is reported. First, a simulation based on optical matrices with an incident Gaussian beam was performed. The incident Gaussian beam is decomposed into multiple plane waves and then propagated through the simulated Fabry–Perot cavity made of silicon-air layered DBRs (see Fig. (3b)). Fig. 8 shows the comparison between simulated and experimental results on the same graphic. The simulated result, dashed line, is in good agreement with the measured spectrum, plain line, for this 35 μm long cavity gap. Properties of these resonance peaks were calculated from the experimental and simulated spectra and are reported in Table I, where FWHM is the Full Width at Half Maximum, FSR is the Free Spectral Range and the finesse is $\mathrm{FSR}/\mathrm{FWHM}$. Differences between experimental and simulated spectra properties are mainly due to the simulated roughness of the interfaces. The simulated roughness, approximated as an absorption layer, affects the sharpness of resonance peaks. It lowers the intensity at the resonant wavelength, increases the FWHM value and thus yields a smaller finesse. Furthermore, simulations do not accommodate for light re-entering the cavity from reflections elsewhere on the device and neither for multimode resonance nor multimode coupling behavior.

As mentioned previously, a rib waveguide coupled to a Fabry–Perot cavity can be used in a resonant spectroscopic measurement. This technique enables detection of small variations of refractive index. Although, before handling biological cells measurement, characterization of the sensor response with homogeneous liquids must be performed. The calculated sensitivity, in units of nm per Refractive Index Unit (RIU), was derived from the peak displacement for different certified refractive index oils. Fig. 9 shows the graphical linear fit with the measurement points used to obtain this value of 1392 nm/RIU. Measurements on the resonance wavelength position had a standard variation of $\sigma = 0.005$ nm corresponding to a detection limit of $3\sigma = 0.015$ nm. Considering this detection limit and the sensitivity, this sensor has a resolution of $\Delta n = 1.1 \times 10^{-5}$. This high resolution over the refractive index could represent a discriminant parameter when measuring biological cells.

VI. CONCLUSION

In summary, we have presented results for optical rib waveguides with very large cross-sections supporting the hypothesis that single-mode behavior is better suited for resonant spectroscopy measurement, especially for sensing application. Achieving single-mode propagation in these waveguides may not be as easy as following the previously established design rules. Therefore, caution must be taken when dealing with very large cross-section optical rib waveguides. Indeed, mutimode rib waveguides tend to hide the resonance peak when coupled to a resonator. Conditions for a single-mode optical rib waveguide were found by modal simulation and experimentally tested for a stand-alone rib waveguide as well as for an on-chip in-plane Fabry–Perot resonant cavity coupled structure. Resonance properties for single-mode behavior were evaluated and employed in a simple refractive index sensor device with homogeneous liquids.

ACKNOWLEDGMENT

The authors would like to thank R. St-Gelais for sharing simulation code and the Microfabrication Laboratory at Polytechnique Montreal for helpful insight in microfabrication.

REFERENCES

[1] A. Densmore *et al.*, "A silicon-on-insulator photonic wire based evanescent field sensor," *IEEE Photon. Technol. Lett.*, vol. 18, no. 23, pp. 2520–2522, Dec. 2006.

[2] T. Claes, W. Bogaerts, and P. Bienstman, "Vernier-cascade label-free biosensor with integrated arrayed waveguide grating for wavelength interrogation with low-cost broadband source," *Opt. Lett.*, vol. 36, no. 17, pp. 3320–3322, 2011.

[3] C. J. Smith *et al.*, "Sensing nitrous oxide with QCL-coupled silicon-on-sapphire ring resonators," *Opt. Exp.*, vol. 23, no. 5, pp. 5491–5499, 2015.
[4] A. Leblanc-Hotte, R. St-Gelais, and Y.-A. Peter, "Optofluidic device for high resolution volume refractive index measurement of single cell," in *Proc. 16th Int. Conf. Miniaturized Syst. Chem. Life Sci.*, 2012, pp. 1330–1332.
[5] R. A. Soref, J. Schmidtchen, and K. Petermann, "Large single-mode rib waveguides in GeSi and Si-on-SiO2," *J. Quantum Electron.*, vol. 27, no. 8, pp. 1971–1974, Aug. 1991.
[6] S. P. Pogossian, L. Vescan, and A. Vonsovici, "The single-mode condition for semiconductor rib waveguides with large cross section," *J. Lightw. Technol.*, vol. 16, no. 10, pp. 1851–1853, Oct. 1998.
[7] J. Lousteau *et al.*, "The single-mode condition for silicon-on-insulator optical rib waveguides with large cross section," *J. Lightw. Technol.*, vol. 22, no. 8, pp. 1923–1929, Aug. 2004.
[8] R. St-Gelais, A. Poulin, and Y.-A. Peter, "Advances in modeling, design, and fabrication of deep-etched multilayer resonators," *J. Lightw. Technol.*, vol. 30, no. 12, pp. 1900–1908, Jun. 2012.

Antoine Leblanc-Hotte received the B.Sc. and M.Sc. degrees in engineering physics from the École Polytechnique de Montréal, Montréal, QC, Canada, in 2010 and 2012, respectively. He is currently working toward the Ph.D. degree in engineering physics at École Polytechnique de Montréal under the direction of Professor Y. Peter. His research interest includes optical resonant cavities for biological sensing applications, optical waveguide propagation, microfluidics, and silicon microfabrication. He received the NSERC Postgraduate Scholarships-Doctoral Program in 2014, the NSERC-CREATE Training Program in Integrated Sensor Systems in 2013, and the NSERC Undergraduate Student Research Award in 2010.

Jean-Sébastien Delisle received the M.D. degree from McGill University, Montréal, QC, Canada, in 1999 and the Ph.D. degree in biomedical sciences from the Université de Montréal, Montréal, in 2010. From 2002 to 2004, he was a Hematology Fellow at McGill University. From 2006 to 2008, he was a Clinical Fellow in Hematopoietic cells transplantation at the Hôpital Maisonneuve-Rosemont, Université de Montréal. He is currently an Assistant Professor in the Department of Medicine, Centre de Recherche de l'Hôpital Maisonneuve-Rosemont, Université de Montréal. His research interests include the study of immune cells and cell imaging techniques to evaluate cell differentiation and function. He received the Junior 1 Salary Award from the Fonds de recherche du Québec–Santé in 2011, the Canadian Institutes of Health Research Clinician-Scientist Formation Award in 2006, the Fonds de recherche du Québec–Santé and Secrétariat du Sang Training Award in 2004, and the McGill University Elizabeth Ann Munro Gordon Prize–Professionalism and Leadership in 1999.

Sylvie Lesage received the Ph.D. degree in experimental medicine with specialization in immunology from the McGill University, Montréal, QC, Canada, in 2000. She subsequently completed the postdoctoral training from the Australian National University, Canberra, A.C.T., Australia, and the Université de Montréal, Montréal, Canada, in 2002 and 2005 respectively. In 2005, she joined the Department of Microbiology and Immunology, Université de Montréal, where she is currently an Associate Research Professor. Her research laboratory is based at the Maisonneuve-Rosemont Hospital Research Center, Canada, and her research program aims at defining homeostatic regulation of cell populations composing the immune system and to identify their impact on the susceptibility of complex genetic diseases such as autoimmune diseases and cancer. She holds a Senior level scholarship from the Fonds de recherche du Québec–Santé since 2015. She previously received the Canadian Institutes of Health Research New Investigator Award in 2010, and the Fonds de recherche du Québec–Santé Junior Investigator Level 1 in 2007.

Yves-Alain Peter (S'93–M'03–SM'07) received the M.Sc. degree in physics and the Dr.Sc. degree from the University of Neuchâtel, Neuchâtel, Switzerland, in 1994 and 2001, respectively. In 1995, he joined the Department of Medical Radiobiology as a Research Associate, Paul Scherrer Institute, Villigen, Switzerland. From 1995 to 2001, he was a Graduate Research Assistant with the Applied Optics Group, Institute of Microtechnology, University of Neuchâtel. From 2001 to 2003, he was a Postdoctoral Researcher with the Microphotonics Group, Stanford University. From 2003 to 2004, he was a Research and Development Engineer and a Project Leader with the Swiss Center for Electronics and Microtechnology, Neuchâtel. In 2004, he joined the Ecole Polytechnique de Montréal, Montréal, Canada, where he is currently a Professor of Engineering Physics. His current research interests include microphotonics and microoptoelectro-mechanical systems.